The Astrophysical Journal, 834:135 (10pp), 2017 January 10 doi:10.3847/1538-4357/834/2/135

BULGE-FORMING GALAXIES WITH AN EXTENDED ROTATING DISK AT $z \sim 2$

Ken-ichi Tadaki[1], Reinhard Genzel[1,2,3], Tadayuki Kodama[4,5], Stijn Wuyts[6], Emily Wisnioski[1], Natascha M. Förster Schreiber[1], Andreas Burkert[1,7], Philipp Lang[1], Linda J. Tacconi[1], Dieter Lutz[1], Sirio Belli[1], Richard I. Davies[1], Bunyo Hatsukade[4], Masao Hayashi[4], Rodrigo Herrera-Camus[1], Soh Ikarashi[8], Shigeki Inoue[9,10], Kotaro Kohno[11,12], Yusei Koyama[13], J. Trevor Mendel[1,7], Kouichiro Nakanishi[4,5], Rhythm Shimakawa[5], Tomoko L. Suzuki[5], Yoichi Tamura[11], Ichi Tanaka[13], Hannah Übler[1], and Dave J. Wilman[1,7]
[1] Max-Planck-Institut für extraterrestrische Physik (MPE), Giessenbachstr., D-85748 Garching, Germany; tadaki@mpe.mpg.de
[2] Department of Physics, Le Conte Hall, University of California, Berkeley, CA 94720, USA
[3] Department of Astronomy, Hearst Field Annex, University of California, Berkeley, CA 94720, USA
[4] National Astronomical Observatory of Japan, 2-21-1 Osawa, Mitaka, Tokyo 181-8588, Japan
[5] Department of Astronomical Science, SOKENDAI (The Graduate University for Advanced Studies), Mitaka, Tokyo 181-8588, Japan
[6] Department of Physics, University of Bath, Claverton Down, Bath, BA2 7AY, UK
[7] Universitäts-Sternwarte Ludwig-Maximilians-Universität (USM), Scheinerstr. 1, München, D-81679, Germany
[8] Kapteyn Astronomical Institute, University of Groningen, P.O. Box 800, 9700AV Groningen, The Netherlands
[9] Kavli Institute for the Physics and Mathematics of the Universe (WPI), UTIAS, The University of Tokyo, Chiba 277-8583, Japan
[10] Department of Physics, The University of Tokyo, 7-3-1 Hongo, Bunkyo, Tokyo 113-0033, Japan
[11] Institute of Astronomy, The University of Tokyo, 2-21-1 Osawa, Mitaka, Tokyo 181-0015, Japan
[12] Research Center for the Early Universe, The University of Tokyo, 7-3-1 Hongo, Bunkyo, Tokyo 113-0033, Japan
[13] Subaru Telescope, National Astronomical Observatory of Japan, 650 North A'ohoku Place, Hilo, HI 96720, USA
Received 2016 August 17; revised 2016 October 13; accepted 2016 October 24; published 2017 January 9

ABSTRACT

We present 0.″2-resolution Atacama Large Millimeter/submillimeter Array observations at 870 μm for 25 Hα-seleced star-forming galaxies around the main sequence at $z = 2.2$–2.5. We detect significant 870 μm continuum emission in 16 (64%) of these galaxies. The high-resolution maps reveal that the dust emission is mostly radiated from a single region close to the galaxy center. Exploiting the visibility data taken over a wide *uv* distance range, we measure the half-light radii of the rest-frame far-infrared emission for the best sample of 12 massive galaxies with $\log(M_*/M_\odot) > 11$. We find nine galaxies to be associated with extremely compact dust emission with $R_{1/2,870\ \mu\mathrm{m}} < 1.5$ kpc, which is more than a factor of 2 smaller than their rest-optical sizes, $\langle R_{1/2,1.6\ \mu\mathrm{m}}\rangle = 3.2$ kpc, and is comparable with optical sizes of massive quiescent galaxies at similar redshifts. As they have an exponential disk with Sérsic index of $\langle n_{1.6\ \mu\mathrm{m}}\rangle = 1.2$ in the rest-optical, they are likely to be in the transition phase from extended disks to compact spheroids. Given their high star formation rate surface densities within the central 1 kpc of $\langle \Sigma\mathrm{SFR}_{1\ \mathrm{kpc}}\rangle = 40\ M_\odot\ \mathrm{yr}^{-1}\ \mathrm{kpc}^{-2}$, the intense circumnuclear starbursts can rapidly build up a central bulge with $\Sigma M_{*,1\ \mathrm{kpc}} > 10^{10}\ M_\odot\ \mathrm{kpc}^{-2}$ in several hundred megayears, i.e., by $z \sim 2$. Moreover, ionized gas kinematics reveal that they are rotation supported with an angular momentum as large as that of typical star-forming galaxies at $z =$ 1–3. Our results suggest that bulges are commonly formed in extended rotating disks by internal processes, not involving major mergers.

Key words: galaxies: evolution – galaxies: high-redshift – galaxies: ISM

1. INTRODUCTION

In the current paradigm of galaxy evolution, galaxies grow mainly by internal star formation along a fairly tight relationship between stellar mass and star formation (so-called main sequence), at a rate that is set by the balance between gas accretion from the cosmic web, internal star formation, and outflows driven by active galactic nuclei (AGNs), supernovae, and massive stars (Bouché et al. 2010; Davé et al. 2012; Lilly et al. 2013). Once galaxy masses reach the Schechter mass, $\log(M_*/M_\odot) \sim 10.9$ (e.g., Marchesini et al. 2009; Ilbert et al. 2013; Muzzin et al. 2013), star formation appears to drop within a short timescale of ∼1 Gyr (Whitaker et al. 2013; Belli et al. 2015; Mendel et al. 2015; Onodera et al. 2015), and galaxies transition to the passive population below the main sequence.

Star-forming galaxies on the main sequence have exponential optical light and mass distributions (e.g., Wuyts et al. 2011b; Whitaker et al. 2015), with orbital motions dominated by rotation in ∼70% of the massive star-forming galaxy population (e.g., Förster Schreiber et al. 2009; Law et al. 2009; Swinbank et al. 2012; Wisnioski et al. 2015; Price et al. 2016; Stott et al. 2016). However, high-redshift star-forming galaxies exhibit significant random motions (turbulent) such that the disks are hot and geometrically thick (van der Wel et al. 2014a; Wisnioski et al. 2015). In contrast, quiescent galaxies are more compact and cuspy than the star-forming galaxies at a given mass, at all redshifts (Bell et al. 2012; Lang et al. 2014; van der Wel et al. 2014b). Given these findings, quenching of star formation must be accompanied by significant structural change, from extended exponential distributions to more compact and more cuspy ones.

To explain the morphological transformation, two main evolutionary paths have been proposed in the literature. A slow cosmological path naturally follows from the strong redshift evolution of galaxy sizes, $R \propto (1+z)^{-1}$ (Mosleh et al. 2012; Newman et al. 2012; van der Wel et al. 2014b; Shibuya et al. 2015). Star-forming galaxies quench star formation and add to the passive population with approximately the same size in a later epoch (van Dokkum et al. 2015; Lilly & Carollo 2016). A second, fast path involves a downward transition in the mass–size plane, at approximately constant

redshift (Barro et al. 2013, 2014; Dekel & Burkert 2014; Zolotov et al. 2015). This process requires a substantial "compaction" of the formally extended star-forming galaxies. One possible mechanism would be a major merger, which is known from observations and simulations to lead to substantial angular momentum redistribution, orbit reconfiguration, and mixing (Mihos & Hernquist 1996; Wuyts et al. 2010). Another possibility is an internal angular momentum redistribution within the star-forming disk. This process has been considered to be effective at high redshift (Noguchi 1999; Immeli et al. 2004a, 2004b; Elmegreen et al. 2008; Genzel et al. 2008; Bournaud et al. 2011), when galaxies are gas rich (Tacconi et al. 2013) and effective viscous dissipation leads to radial inward transport of gas and stars with a timescale of a few hundred megayears (Dekel et al. 2009) and buildup of a central dense core (bulge component) through circumnuclear concentration of gas. Nelson et al. (2016b) find in massive galaxies at $z \sim 1.4$ that central 1 kpc regions are highly attenuated by dust and are responsible for half of the total star formation rate (SFR). In conjunction with morphological quenching (Martig et al. 2009; Genzel et al. 2014a), and powerful AGN outflows (Bower et al. 2006; Croton et al. 2006; Förster Schreiber et al. 2014; Genzel et al. 2014b), the compaction process may then lead to an inside-out quenching near the Schechter mass (Tacchella et al. 2015, 2016).

In this paper, we report observations of submillimeter dust continuum emission with the Atacama Large Millimeter/submillimeter Array (ALMA) to search for compact concentrations of interstellar medium as a unique telltale sign of the fast evolutionary path. An advantage of our study is that there is no selection bias in galaxy morphologies. Therefore, the key goal is to address the issue of morphological transformation from extended exponential disks to quiescent spheroids using the high-resolution ALMA/870 μm maps. We show that bulges can be formed in massive extended, rotating disks at $z \sim 2$, in a short timescale of several hundred megayears (Section 4).

We assume a Chabrier initial mass function (IMF; Chabrier 2003) and adopt cosmological parameters of $H_0 = 70\,\mathrm{km\,s^{-1}\,Mpc^{-1}}$, $\Omega_M = 0.3$, and $\Omega_\Lambda = 0.7$.

2. HIGH-RESOLUTION 870 μm IMAGING

2.1. Sample Selection

Our sample is selected from a narrowband imaging survey with the MOIRCS on the Subaru Telescope, tracing Hα emission at $z = 2.19 \pm 0.02$ or 2.53 ± 0.02 (Kodama et al. 2013; Tadaki et al. 2013), in the SXDF-UDS-CANDELS field, where 0.″18-resolution *Hubble Space Telescope* (*HST*) images at four passbands (V_{606}, I_{814}, J_{125}, and H_{160}) are publicly available (Grogin et al. 2011; Koekemoer et al. 2011). The limiting Hα line fluxes for the narrowband survey correspond to dust-uncorrected SFRs of 4 $M_\odot\,\mathrm{yr^{-1}}$ at $z = 2.19$ and 10 $M_\odot\,\mathrm{yr^{-1}}$ at $z = 2.53$ (Kennicutt 1998). Interlopers with a different emission line such as [O III] at $z \sim 3$ are excluded by utilizing colors to pick up the Balmer/4000 Å break (Suzuki et al. 2015). Follow-up spectroscopic observations demonstrate that our method robustly picks up only galaxies at the redshift range of interest (Tadaki et al. 2011, 2013). For ALMA observations of 25 galaxies, we prioritize bright objects in MIPS 24 μm maps, which are taken from the SpUDS Spitzer Legacy program (PI: James Dunlop), to increase the feasibility of detection in the ALMA Early Science phase. Four out of 25 galaxies are not detected at 24 μm.

2.2. Galaxy Properties

To derive galaxy properties, we use the 3D-*HST* catalog, including photometric data at 18 bands from *U* band to 8.0 μm (Skelton et al. 2014; Momcheva et al. 2016). Using the FAST code (Kriek et al. 2009), we perform spectral energy distribution (SED) fitting with stellar population synthesis models of Bruzual & Charlot (2003) under a solar metallicity, exponentially declining star formation histories (SFHs), and the dust attenuation law of Calzetti et al. (2000) to estimate stellar masses. We also create a deep PACS 160 μm map from archival data with UNIMAP (Piazzo et al. 2015) and extract sources on the basis of 24 μm priors (see also Lutz et al. [2011] for the methodology). Following the recipes of Wuyts et al. (2011a), we compute total SFRs from a combination of the rest-frame 2800 Å and infrared luminosities with PACS 160 μm or MIPS 24 μm fluxes (L_{IR}). For four galaxies without detection at mid-infrared, we use Hα-based SFRs with dust correction from SED modeling (Tadaki et al. 2015). Table 1 summarizes the galaxy properties for our ALMA sample of 25 galaxies. We adopt uncertainties of $\pm$0.15 dex for the stellar mass and $\pm$0.20 dex for the SFR taking into account systematic errors although uncertainties associated with photometry measurements are somewhat smaller (Wuyts et al. 2011a). For dusty star-forming galaxies such as submillimeter sources, the random uncertainties in the stellar mass estimates could be larger because the stellar components hide behind dust.

SFRs of galaxies are well correlated with their stellar masses, with a scatter of $\pm$0.3 dex (e.g., Daddi et al. 2007; Elbaz et al. 2007; Noeske et al. 2007; Pannella et al. 2009; Rodighiero et al. 2011; Whitaker et al. 2012, 2014; Kashino et al. 2013; Shivaei et al. 2015; Tasca et al. 2015). Our ALMA sample of 25 galaxies is on/around the star formation main sequence (Figure 1), indicating that they probe the normal star-forming population at $z \sim 2$.

At $z = 2.2$–2.5, *HST*/WFC3 H_{160} band traces the rest-optical light ($\lambda_{\mathrm{rest}} = 0.46$–$0.50$ μm) of galaxies. Structural parameters such as circularized half-light radius and Sérsic index are derived with GALFIT (Peng et al. 2010) in the H_{160}-band maps (van der Wel et al. 2012, 2014b). We do not use U4-27289 and U4-16795 for optical size arguments because the best-fit Sérsic index reached the constrained limit ($n = 8.0$ or $n = 0.2$).

2.3. ALMA Observations

We have carried out ALMA observations for 25 galaxies on the main sequence at $z = 2$ with 32–49 antennas and baseline lengths of 20–1600 m. On-source time is 6–8 minutes per object. We use the band 7 receivers with the 64-input correlator in Time Division Mode in a central frequency of 345 or 350 GHz (~870 μm). We utilize the Common Astronomy Software Application package (CASA; McMullin et al. 2007) for the data calibration. We reconstruct two kinds of clean maps: low-resolution maps with *uv*-taper of the on-sky FWHM = 0.″5 and high-resolution ones with natural weighting. The synthesized beam sizes are 0.″47–0.″54 and 0.″15–0.″21, respectively. We measure total fluxes, S_{aper}, with a 1.″5 aperture photometry in the low-resolution maps or with a 1.″0 aperture in the high-resolution maps. Uncertainties of total

Table 1
Galaxy Properties for Our ALMA Sample of 25 SFGs

3D-*HST* ID (Skelton+14)	z_{NB}[a]	log M_*[b] ($M_\odot$)	log SFR[b] ($M_\odot$ yr^{-1})	SN$R_{0.5}$[c]	SN$R_{0.2}$[c]	S_{aper}[c] (mJy)	S_{model}[d] (mJy)	$R_{1/2}$[d] (arcsec)	$R_{1/2,cor}$[e] (arcsec)	v_{rot}/σ_0[f]
U4-13952	2.19	11.33	2.25	13.4	7.9	2.51 ± 0.31	2.94 ± 0.55	0.24 ± 0.04	0.28 ± 0.06	3.8 ± 1.3
U4-34817	2.19	11.26	2.36	7.8	5.4	1.73 ± 0.28	2.13 ± 0.78	0.31 ± 0.10	0.38 ± 0.12	Hα detection
U4-20704	2.19	11.46	2.36	8.1	6.3	3.00 ± 0.40	4.28 ± 1.11	0.44 ± 0.10	0.48 ± 0.11	4.2 ± 1.4
U4-28702	2.19	11.03	2.10	10.1	9.7	1.73 ± 0.36	1.64 ± 0.31	0.10 ± 0.02	0.13 ± 0.03	···
U4-36568	2.19	11.02	2.49	4.0	<5.0	0.71 ± 0.24	···	···	···	5.3 ± 1.8
U4-24247	2.19	10.71	1.98	4.4	<5.0	1.09 ± 0.36	···	···	···	Hα detection
U4-32171	2.19	10.71	2.15	<4.0	<5.0	···	···	···	···	···
U4-11582	2.19	10.83	2.01	<4.0	<5.0	···	···	···	···	6.9 ± 2.4
U4-27289	2.19	10.78	1.78	<4.0	<5.0	···	···	···	···	···
U4-36247	2.19	11.07	2.42	13.5	16.0	1.80 ± 0.24	1.41 ± 0.18	0.05 ± 0.01	0.07 ± 0.02	3.5 ± 2.3
U4-32351	2.19	11.05	2.18	6.5	6.8	0.95 ± 0.26	0.74 ± 0.24	0.10 ± 0.04	0.17 ± 0.08	5.2 ± 0.9
U4-18807	2.19	10.98	1.86	<4.0	5.5	0.58 ± 0.26	···	···	···	7.1 ± 4.9
U4-27939	2.19	10.60	2.06	<4.0	<5.0	···	···	···	···	···
U4-14574	2.19	10.59	1.99	4.0	<5.0	1.20 ± 0.46	···	···	···	···
U4-15198	2.53	10.93	2.24	<4.0	<5.0	···	···	···	···	···
U4-16795	2.53	11.26	2.62	31.0	29.2	4.59 ± 0.31	4.46 ± 0.27	0.12 ± 0.01	0.13 ± 0.01	···
U4-34138	2.53	11.00	2.24	9.7	11.4	1.60 ± 0.29	1.10 ± 0.19	0.06 ± 0.02	0.08 ± 0.03	3.8 ± 2.0
U4-28473	2.53	11.31	2.59	26.0	22.5	4.87 ± 0.45	5.12 ± 0.39	0.13 ± 0.01	0.14 ± 0.02	6.1 ± 4.0
U4-33135	2.53	11.02	2.07	8.6	9.8	1.47 ± 0.34	1.27 ± 0.25	0.07 ± 0.02	0.09 ± 0.03	···
U4-27046	2.53	10.83	2.41	<4.0	<5.0	···	···	···	···	Hα detection
U4-16504	2.53	11.25	2.37	20.4	15.7	2.82 ± 0.23	3.16 ± 0.34	0.15 ± 0.02	0.17 ± 0.03	···
U4-11780	2.53	10.42	1.93	<4.0	<5.0	···	···	···	···	···
U4-13197	2.53	10.94	1.55	<4.0	<5.0	···	···	···	···	···
U4-34617	2.53	11.04	2.42	10.6	13.0	1.67 ± 0.28	0.93 ± 0.13	0.02 ± 0.01	0.04 ± 0.02	···
U4-14870	2.53	10.50	1.63	<4.0	<5.0	···	···	···	···	···

Notes.
[a] Redshifts derived from the narrowband imaging survey with Subaru (Tadaki et al. 2013).
[b] Stellar masses estimated with SED modeling and total SFRs computed from rest-frame 2800 Å and infrared luminosities (Wuyts et al. 2011a). We adopt uncertainties of ±0.15 dex for the stellar mass and ±0.20 dex for the SFR.
[c] Signal-to-noise ratios of the peaks in 0.″5- (LR) and 0.″2-resolution (HR) ALMA/870 μm maps. We measure total fluxes, S_{aper}, with a 1.″5 aperture in the LR maps or with a 1.″0 aperture in the HR maps.
[d] 870 μm fluxes and half-light radii for the best-fit exponential model.
[e] Half-light radii corrected for residual emission with S_{extra} = 0.4 mJy (Section 3.2).
[f] Ratios of rotation velocity to local velocity dispersion measured with KMOS.

fluxes are derived by computing standard deviations of 50 random apertures in each of the maps. The rms levels are 98–142 μJy beam^{-1} for the low-resolution maps and 56–74 μJy beam^{-1} for the high-resolution maps.

For detections, we adopt a 4σ threshold in a peak flux density on the low-resolution maps or 5σ on the high-resolution maps, where sources with negative signal become zero. We have detected 16 out of the 25 galaxies either in the low-resolution or the high-resolution maps. Massive and active star-forming galaxies tend to be bright at 870 μm (Figure 1). For galaxies at similar redshifts (z = 2.19 or 2.53), we find the measured 870 μm fluxes to be correlated with both stellar masses and SFRs (Figure 2). The Pearson product-moment correlation coefficients are 0.66 for stellar masses and 0.69 for SFRs. The detection rate is 100% (13/13) in the stellar mass range of $\log(M_*/M_\odot) > 11$, while some galaxies with high SFRs are not detected. Given the correlation and the mass dependence of the detection rate, stellar masses are likely to be a good predictor of 870 μm fluxes (Dunlop et al. 2016). The total average flux is $\langle S_{aper} \rangle$ = 2.0 mJy (0.6–4.9) in all detected objects, fainter than those of classical submillimeter galaxies identified by single-dish telescopes (e.g., Simpson et al. 2015).

2.4. KMOS Observations

We have observed 12 of 25 galaxies with the near-infrared integral-field spectrometer KMOS on the Very Large Telescope (VLT) as part of the KMOS^{3D} survey (Wisnioski et al. 2015) to study the spatially resolved ionized gas kinematics of these sources. For our ALMA sample, a typical integration time is 11 hr. We reduced the data with the Software Package for Astronomical Reduction (SPARK; Davies et al. 2013). All of our targets show Hα emission and are spectroscopically confirmed to be at z = 2.19 or z = 2.53 within the expected uncertainty from the width of the narrowband filters (Δz = ±0.02).

Our method to derive kinematic parameters is described in detail by Burkert et al. (2016; see also Wisnioski et al. 2015; Wuyts et al. 2016). Here, we summarize procedures to obtain the rotation velocity (v_{rot}), the local velocity dispersion (σ_0), and the disk angular momentum (j_{disk}) from the reduced 3D cubes. A fundamental assumption is that high-redshift star-forming galaxies are symmetric oblate, thick disks with an exponential profile, which is supported by observations (Förster Schreiber et al. 2009; Law et al. 2009; Wuyts et al. 2011b; Genzel et al. 2014a; van der Wel et al. 2014a). First, we create velocity field and velocity dispersion maps by fitting

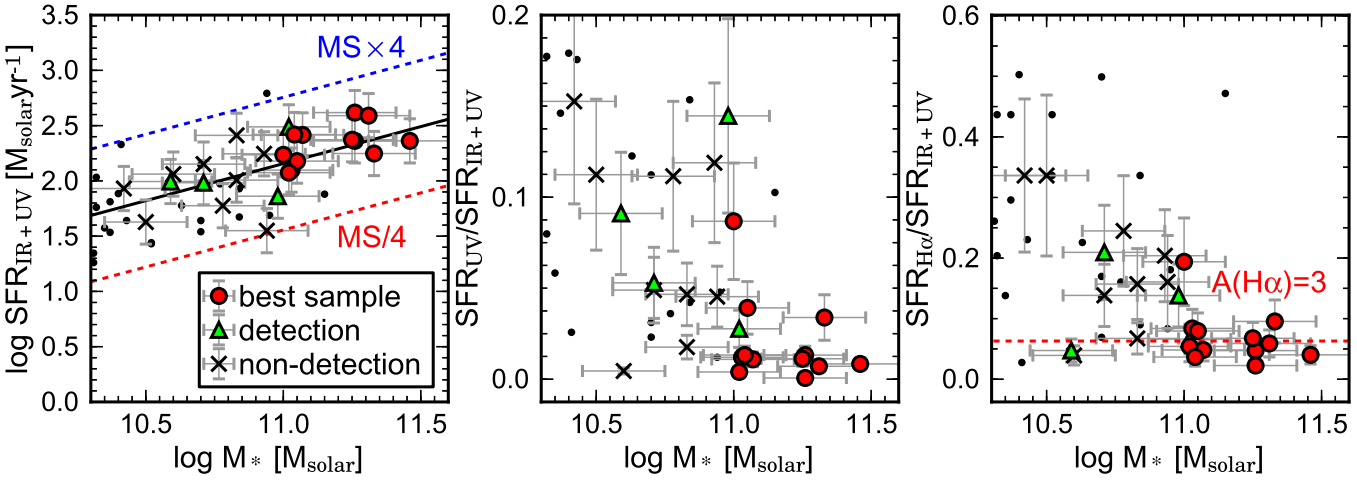

Figure 1. Left: stellar mass vs. SFR for our ALMA sample of 25 star-forming galaxies at $z = 2.2$ or $z = 2.5$. Red circles indicate the best sample that is detected in both the low-resolution and high-resolution 870 μm maps, and green triangles show all objects detected in either map. Small dots show our parent sample of galaxies identified by the narrowband Hα imaging. They lie on/around the main sequence of star formation at $z = 2.0$–2.5 (solid line; Whitaker et al. 2014). Middle: ratio of the UV-based SFR over the total one, derived from UV and infrared luminosities, as a function of stellar mass. Right: ratio of the Hα-based SFR over the total one. Hα fluxes are measured in the narrowband maps (Tadaki et al. 2013). A dashed red line corresponds to a dust extinction of $A_{H\alpha} = 3$ mag.

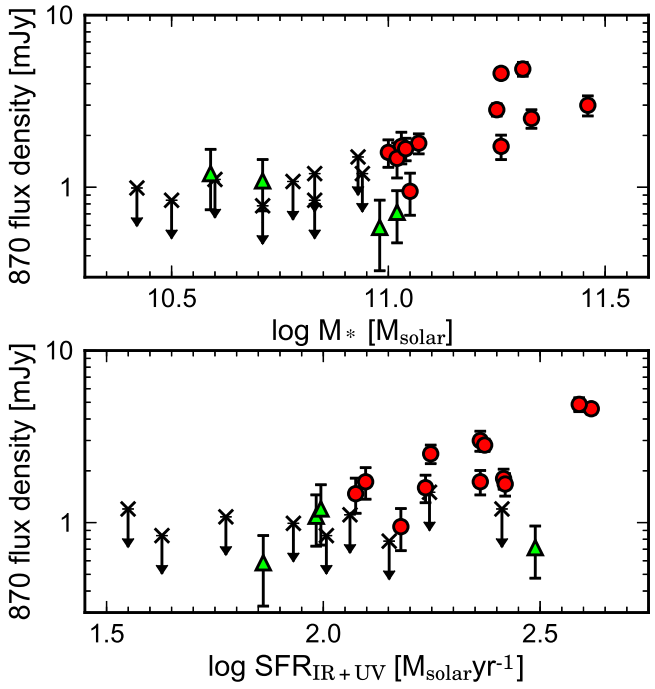

Figure 2. Comparisons between 870 μm fluxes and galaxy properties. Symbols are the same as in Figure 1. For nondetected objects, the 3σ upper limits are plotted.

Gaussian profiles to the data in each spatial pixel. After determining the largest total velocity gradient and the radius at which this velocity gradient reaches a maximum value (R_{max}), we measure rotation velocities at R_{max} and local velocity dispersions in outer disks. Here we correct for observational effects (inclination and beam smearing) on the basis of structural parameters for the rest-optical light in the H_{160}-band maps. For symmetric oblate disks, the inclination, i, is estimated from the projected minor-to-major-axis ratio, $q_{obs} = b/a$, as $\sin^2(i) = (1 - q_{obs}^2)/(1 - q_{int}^2)$, with an intrinsic finite thickness of $q_{int} = 0.15$–0.25 (Förster Schreiber et al. 2009; Law et al. 2009; Wisnioski et al. 2015; Wuyts et al. 2016). The impact of the beam smearing depends on the ratio of half-light radius to half-width at half-maximum (HWHM) of the PSF, $R_{1/2}/R_{PSF}$, and $R_{max}/R_{1/2}$. We also correct for turbulent pressure to derive a circular velocity, v_{circ}, and the correction factor is 1.03–1.32 in our sample. The specific angular momentum of ionized gas is computed as

$$j_{disk} = k_{disk} \times v_{circ} \times R_{1/2}. \quad (1)$$

Here, we take into account deviations from exponential profiles. The correction factors, k_{disk}, are $k_{disk} = 1.19$ in $n = 1$, $k_{disk} = 2.29$ in $n = 4$, and $k_{disk} = 0.89$–1.36 in our sample (Romanowsky & Fall 2012).

We eventually obtain the kinematic parameters for nine galaxies (Table 1). They are all rotation supported with $\langle v_{rot}/\sigma_0 \rangle = 5.1$ (3.5–7.1) as is the case for most galaxies on/around the main sequence (Wisnioski et al. 2015). Therefore, our ALMA sample is a typical star-forming population at $z \sim 2$ in star-forming activity, morphology, and kinematics.

3. SPATIAL EXTENT OF STAR FORMATION WITHIN GALAXIES

The most straightforward way to know the subsequent evolution of galaxy morphologies is to reveal where and how many stars are formed within galaxies at the observed epoch. Many previous studies use the rest-frame UV or Hα maps to investigate the spatial distribution of star formation (e.g., Genzel et al. 2011; Nelson et al. 2012, 2016a; Wuyts et al. 2013). However, for our ALMA sample of massive galaxies, the measured ratios of SFR$_{UV}$/SFR$_{IR+UV}$ and SFR$_{H\alpha}$/SFR$_{IR+UV}$ indicate that ~99% of the total SFR is obscured by dust, and even Hα emission misses 90%–95% of star formation, corresponding to a dust extinction of $A_{H\alpha} \sim 3$ mag (Figure 1). Therefore, the 870 μm maps tracing dust emission itself have a great advantage over Hα in approximately providing the spatial distribution of star formation within galaxies if the dust temperature is constant across galaxies. In this section, exploiting the ALMA data taken in the extended configuration, we study the spatial distributions of star formation within galaxies. We use the best sample of 12 galaxies that are detected in both low-resolution and high-resolution maps because the detections in a wide range of uv distance allow

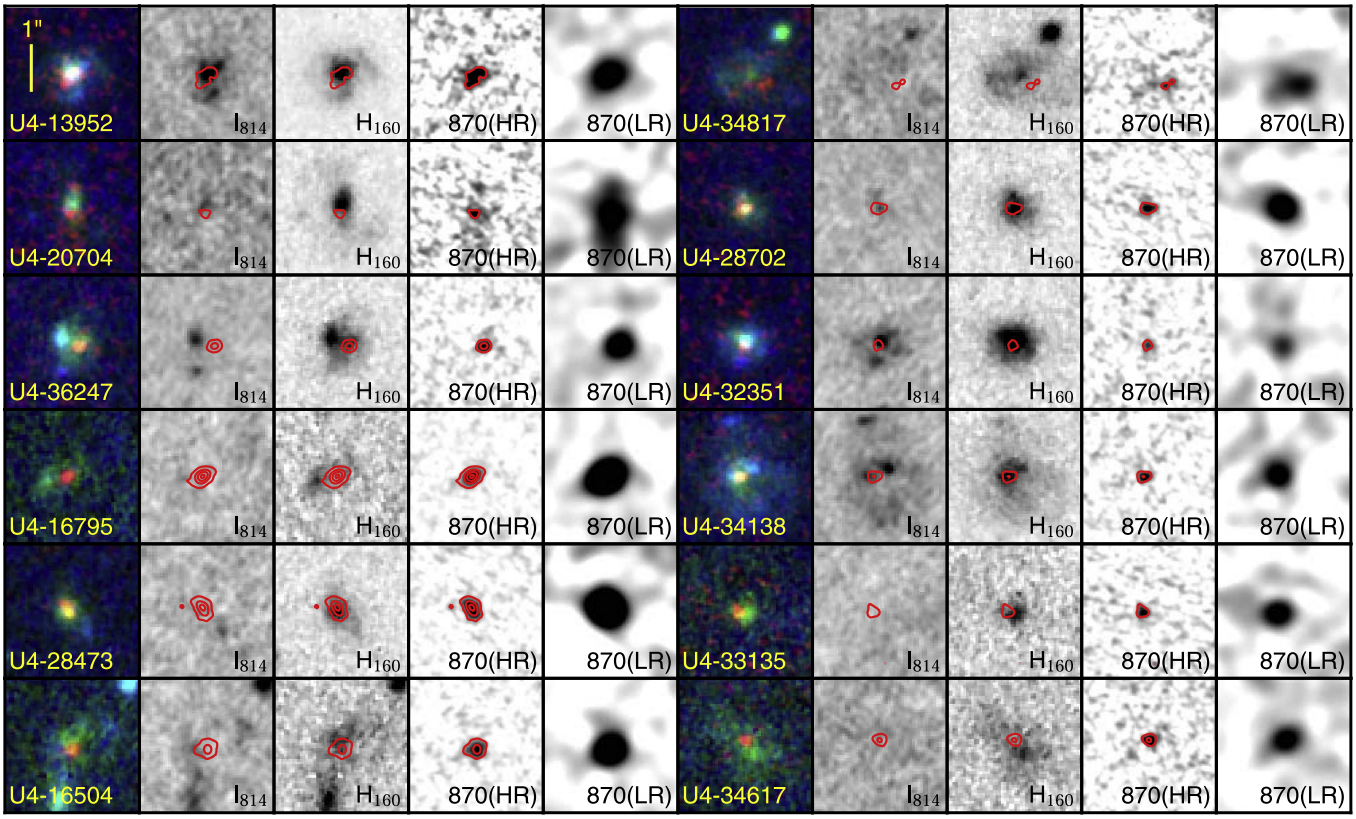

Figure 3. Three-color images with *HST*/I_{814}, H_{160}, and ALMA/870 μm band ($3'' \times 3''$) for our sample of 12 galaxies with 870 μm size measurements. Red contours display the 870 μm flux densities in the high-resolution maps and are plotted every 8σ, starting at 4σ.

us to constrain the spatial extent of dust continuum emission. Using similar spatial resolution maps with *HST*/WFC3, we directly compare dusty star-forming regions with the rest-optical light mainly from stars.

3.1. High-resolution 870 μm Maps

First, we visually inspect the high-resolution 870 μm maps before quantitatively measuring sizes of the dust continuum emission. Figure 3 shows the ALMA maps along with the similar-resolution ACS/I_{814} (rest-UV) and WFC3 H_{160} (rest-optical) light distributions for the 12 galaxies. For about half of our sample, there is very little UV emission, probably due to strong dust extinction. A common remarkable feature is that 870 μm emission is radiated from a single region close to the rest-optical center rather than multiple components like star-forming clumps in disks, seen in the rest-UV or Hα maps. Given that they are highly obscured, the concentrated component at 870 μm is primarily responsible for star formation in the galaxies. An absence of dust emission in UV clumps means that their 870 μm flux density could be below the lower limit of our ALMA observations. Also note that these high-resolution maps are sensitive to compact components with a spatial scale of $\sim 0\farcs2$ and we might miss extended, diffuse components. We assess impacts by faint components and/or extended ones in the next section. For U4-34817 and U4-20704, the 870 μm emission appears to be faint in the high-resolution maps in spite of a relatively large flux ($S_{\rm aper} = 1.7$, 3.0 mJy). They are likely to be associated with extended emission as they are more robustly detected in the low-resolution maps.

3.2. Size Measurements for 870 μm Continuum Emission

We measure half-light radii ($R_{1/2}$) of the primary component for dust emission, identified in the high-resolution maps. As interferometric telescopes do not directly provide images, the Fourier transform must be performed to reconstruct maps (clean algorithm). Then, image properties such as rms level, spatial resolution, and source structures depend on clean parameters. To avoid these uncertainties, we perform visibility fitting with a circular exponential profile as seen in the rest-optical light. In previous studies, a Gaussian model is commonly used for size measurements in the $u-v$ plane (Ikarashi et al. 2015; Simpson et al. 2015; Tadaki et al. 2015). However, a radial profile of galaxy disks is approximately described by an exponential function, $n = 1$ (e.g., Wuyts et al. 2011b). As our concern in this paper is primarily size differences between the rest-optical and 870 μm emission, an exponential model is preferred for a consistent comparison.

For an exponential function in the image plane, $f(R) = \exp(-1.678R/R_{1/2})$, the Hankel transform (equivalent to a two-dimensional Fourier transform) is given by

$$g(u) = S_{\rm model} \times \frac{k_0^3}{(u^2 + k_0^2)^{3/2}}, \quad (2)$$

where $S_{\rm model}$ is the total flux of the model and k_0 is the spatial frequency to characterize a spatial extent. For the visibility fitting, we use the `UVMULTIFIT` tool (Martí-Vidal et al. 2014), which outputs FWHM of a two-dimensional flux distribution (FWHM $= 0.826\ R_{1/2}$). In some cases, unexpected 870 μm sources are serendipitously detected within the primary beam. As they affect the visibility amplitudes of our main targets, we

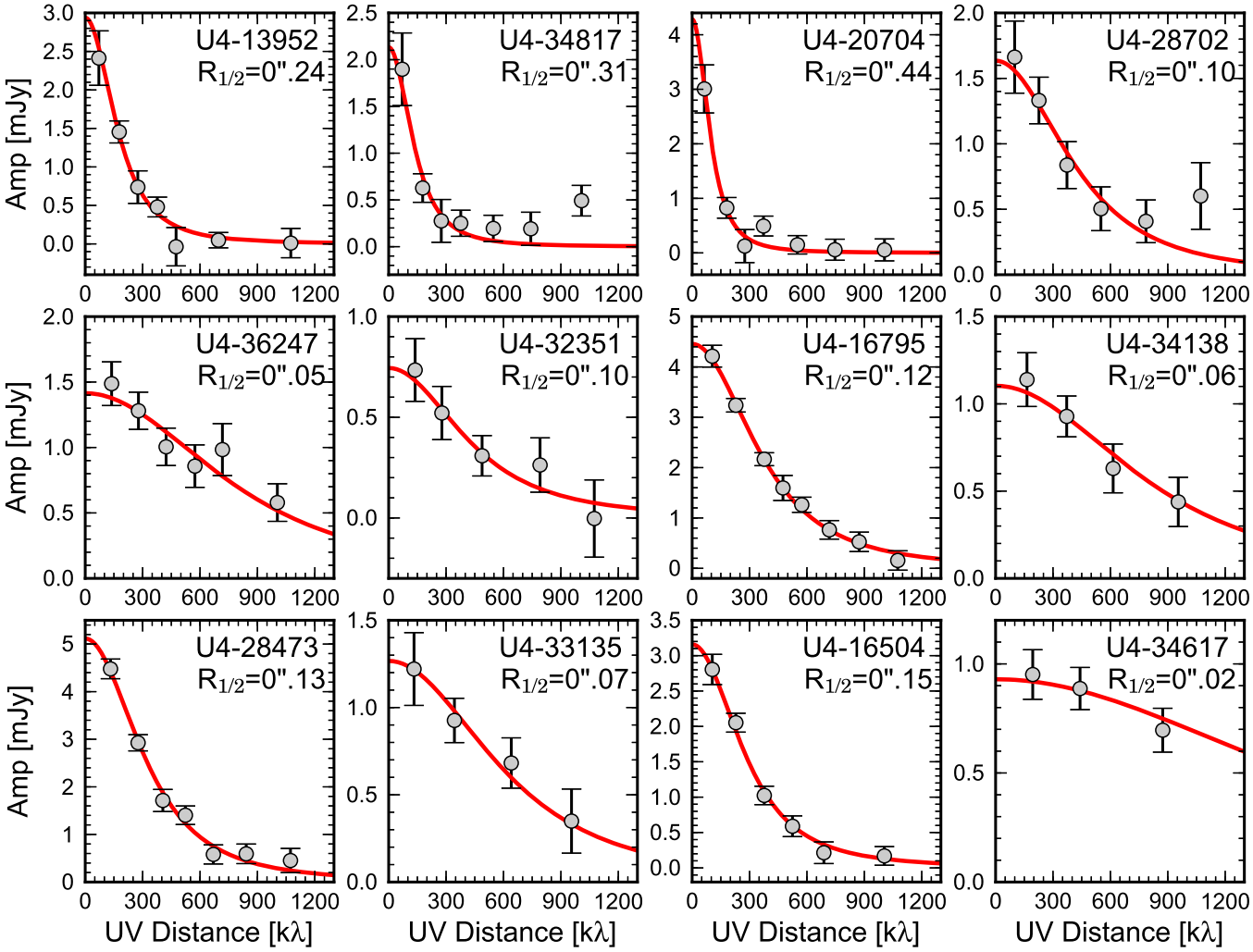

Figure 4. Visibility amplitudes vs. *uv* distances for our sample of 12 galaxies with size measurements. Red lines indicate the best-fitting model, $S_{\rm model} \times k_0^3/(u^2+k_0^2)^{3/2}$. The fitting was done with individual visibilities, not plotted in this figure. For reference, the amplitudes averaged over *uv* distance are shown by gray circles.

create a model of the interlopers and subtract it from the observed visibilities in advance. Figure 4 shows the observed visibility amplitudes after binning and the best-fit models, whose size and flux density are summarized in Table 1. We obtain uncertainties in the sizes from fitting errors. If adopting a circular Gaussian model, the estimated 870 μm sizes would become smaller by 7% $\pm$ 6%.

We also search for systematic positional offsets between ALMA/870 μm and *HST*/1.6 μm centers. There is a small systematic offset of 19 mas in R.A. and 70 mas in declination. U4-34817 has a significant offset of 405 mas between 870 μm and 1.6 μm peak. Except for this galaxy, a mean separation is 130 $\pm$ 68 mas, supporting the notion that the dust continuum emission arises from a central region of the galaxies.

For the size measurements, we investigate the impact of residual emission, which could be due to an additional extended component over entire disks, substructures like clumps, or deviations from an exponential model. In clean maps after subtraction of the best-fit model, no residual emission is detected above 3σ. To increase sensitivity, especially to extended emission, we perform a stacking analysis of the model-subtracted visibilities for nine compact sources, using the STACKER tool (Lindroos et al. 2015). The phase center is shifted to the center position of the best-fit model before the stacking. A clean map is created from the stacked visibility with *uv*-taper of the on-sky FWHM = 1.″0, and the resultant synthesized beam size is 0.″81 × 0.″87. The residual emission is detected at 4.3σ, and its flux density within 2.″0 aperture is $S_{\rm extra}$ = 0.42 mJy, corresponding to 21% of the total average flux.

Conservatively assuming that this residual flux originates outside the half-light radius, we calculate the corrected half-light radius, $R_{1/2,\rm cor}$, which encloses half of the total flux, $S_{1/2,\rm cor}$ = ($S_{\rm model}$ + $S_{\rm extra}$)/2, in the primary exponential component. The amount of correction depends on the ratio of $S_{1/2,\rm cor}/S_{\rm model}$. This has the largest impact on size measurements for U4-32351 with the faintest model flux as $R_{1/2,\rm cor}$ corresponds to a radius enclosing 78% of the flux in the exponential model.

For 9 out of the 12 star-forming galaxies, the corrected 870 μm sizes are less than 1.5 kpc (Figure 5, Table 2), which is more than a factor of 2 smaller than their rest-optical sizes and is comparable to optical sizes of massive quiescent galaxies (e.g., Toft et al. 2007; Trujillo et al. 2007; van Dokkum et al. 2008; Newman et al. 2012). They have an extended exponential profile with $R_{1/2,1.6\,\mu\rm m}$ = 3.2 (1.5–5.8) kpc and

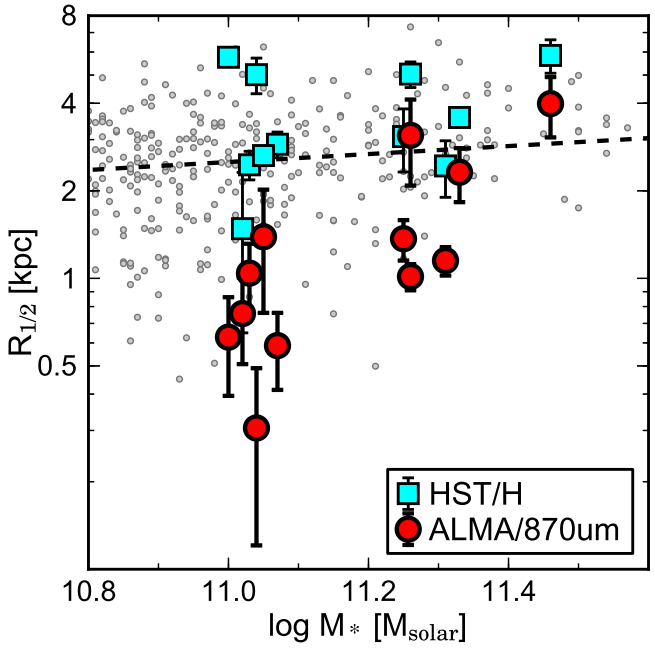

Figure 5. Comparison of circularized half-light radii at ALMA/870 μm (red circles) with those at *HST*/H_{160} band (cyan squares) for our sample of 12 galaxies with size measurements at 870 μm. Gray circles indicate the rest-optical sizes for star-forming galaxies around the main sequence at $z = 1.9$–2.7, which are drawn from the 3D-*HST* survey. A dashed line shows their fitting function, $\log(R_{1/2}) = 0.14\log(M_*) - 1.11$.

Sérsic index $n = 1.2$ (0.5–1.9) in the rest-optical maps. In the stellar mass range of $\log(M_*/M_\odot) < 11$, star-forming galaxies could form stars within somewhat larger disks than the bulk of stars to slowly grow in size with increasing stellar mass as seen in the mass–size relation of normal star-forming galaxies (Nelson et al. 2016a; Rujopakarn et al. 2016). Our best ALMA sample of 12 star-forming galaxies is all massive with $\log(M_*/M_\odot) > 11$. Their individual detection of compact dust emission above the Schechter mass suggests that star formation preferentially occurs in the compact central region. This has a potential to change galaxy morphologies from disk dominated to bulge dominated with high stellar mass surface densities (see next section).

In the analysis of size measurements, we do not include two massive star-forming galaxies with $\log(M_*/M_\odot) > 11$ in the parent sample of galaxies identified by the narrowband survey. One is not observed with ALMA, and the other one (U4-36568) is not detected in the high-resolution map (Figure 1). Given the high completeness of 86% (12/14) in the stellar mass range, our results are not significantly affected by the sample selection. Therefore, we find massive galaxies to commonly form stars in the extremely compact central region as at least 64% (9/14) have small 870 μm sizes of $R_{1/2,870\,\mu\mathrm{m}} < 1.5$ kpc. This result is in excellent agreement with similar and independent evidence coming from an ALMA/870 μm study of six massive star-forming galaxies at $z \sim 2$ (Barro et al. 2016). Barro et al. (2016) find that the mean half-SFR radius is ∼30% smaller than the mean half-mass radius. The main difference between our work and Barro et al. (2016) is that they preselect only optically compact star-forming galaxies while our study almost completely selects main-sequence galaxies.

4. BULGE FORMATION IN EXTENDED, ROTATING DISKS

Given that our ALMA sample is already massive, $\log(M_*/M_\odot) > 11.0$, they are likely to soon thereafter quench the active star formation and to be observed as quiescent galaxies in the local universe. Quiescent galaxies are always smaller than star-forming galaxies at any redshift and any stellar mass and have a cusp profile ($n > 2$) unlike star-forming galaxies with exponential disks (Wuyts et al. 2011b; van der Wel et al. 2014b). A spatial distribution of stars within galaxies would not be changed unless a violent process like major mergers happens. However, centrally concentrated star formation reduces the half-light or half-stellar-mass radii of galaxies, and their Sérsic index would increase by central bulge formation.

We quantitatively assess the possibility of bulge formation in our sample of the 12 massive galaxies with reliable size measurements of dust continuum emission. Quiescent galaxies generally have a dense core with high stellar mass surface densities within 1 kpc of galaxy centers of $\log(\Sigma M_{*,1\,\mathrm{kpc}}/M_\odot\ \mathrm{kpc}^{-2}) = 10$, while star-forming galaxies mostly do not (van Dokkum et al. 2014; Barro et al. 2015). For our sample, we create stellar mass maps by spatially resolved SED modeling with multiband *HST* data (Wuyts et al. 2012; Lang et al. 2014) to calculate stellar mass surface densities within 1 kpc from the 870 μm center. None of the members of our sample satisfy the criterion of a dense core at the current moment (Table 2). The spatial distribution of star formation within galaxies allows us to understand when the dense core is formed by subsequent star formation. Exploiting the geometric information of the best-fit exponential models at 870 μm, we derive the SFR surface densities within the central 1 kpc ($\Sigma\mathrm{SFR}_{1\,\mathrm{kpc}}$) from the *Spitzer*/*Herschel*-based total SFRs over galaxies. For nine galaxies with compact dust emission of $R_{1/2,870\,\mu\mathrm{m}} < 1.5$ kpc, they are intensely forming stars in the central region with $\Sigma\mathrm{SFR}_{1\,\mathrm{kpc}} = 40$ (19–65) $M_\odot\,\mathrm{yr}^{-1}\,\mathrm{kpc}^{-2}$ (Table 2). Then, bulge formation timescales to reach $\log(\Sigma M_{*,1\,\mathrm{kpc}}/M_\odot\,\mathrm{kpc}^{-2}) = 10$ are estimated by

$$\tau_{\mathrm{bulge}} = \frac{10^{10} - \Sigma M_{*,1\,\mathrm{kpc}}}{w \times \Sigma\mathrm{SFR}_{1\,\mathrm{kpc}}}, \quad (3)$$

taking into account mass loss due to stellar winds ($w = 0.6$ in Chabrier IMF; see also van Dokkum et al. 2014). The estimated bulge formation timescales are $\langle\log\tau_{\mathrm{bulge}}\rangle = 8.47$ (8.16–8.79) for the nine galaxies with $R_{1/2,870\,\mu\mathrm{m}} < 1.5$ kpc. They can complete the dense core formation by $z = 2$ when the current level of star formation is maintained for several hundred megayears. Galaxies forming stars in disks as extended as the rest-optical light would have to keep the current star formation for a longer time (∼2 Gyr). This is not consistent with stellar populations obtained in high-redshift quiescent galaxies, where timescales for star formation are $\tau < 1$ Gyr (e.g., Belli et al. 2015; Onodera et al. 2015).

We also estimate gas depletion timescales for our ALMA sample using the Genzel et al. (2015) scaling relations, combining CO-based, *Herschel* far-infrared-dust-based, and submillimeter-dust-based estimates, in order to average over the systematic uncertainties inherently present in all of these techniques. We use the updated version of this scaling relation (L. J. Tacconi et al. 2016, in preparation),

Table 2
Galaxy Properties for 12 SFGs with 870 μm Size Measurements

3D-*HST* ID	$n_{1.6\,\mu m}$ [a]	$R_{1/2,1.6\,\mu m}$ [a] (kpc)	$R_{1/2,870\,\mu m}$ [b] (kpc)	$\log\Sigma M_{*1\,kpc}$ [c] $M_\odot$ kpc^{-2}	$\log\Sigma SFR_{1\,kpc}$ [d] $M_\odot$ yr^{-1} kpc^{-2}	Logτ_{bulge} [e] (yr)	Logτ_{depl} [f] (yr)
U4-13952	2.2 ± 0.2	3.6 ± 0.2	2.3 ± 0.5	9.63 ± 0.15	1.00 ± 0.23	8.96 ± 0.26	8.56 ± 0.31
U4-34817	0.6 ± 0.6	5.0 ± 0.5	3.1 ± 1.0	9.17 ± 0.15	0.93 ± 0.30	9.14 ± 0.30	8.48 ± 0.31
U4-20704	3.4 ± 0.2	5.8 ± 0.8	4.0 ± 0.9	9.83 ± 0.15	0.72 ± 0.26	8.96 ± 0.41	8.55 ± 0.31
U4-28702	1.2 ± 0.5	2.5 ± 0.3	1.0 ± 0.3	9.45 ± 0.15	1.28 ± 0.22	8.79 ± 0.23	8.52 ± 0.31
U4-36247	0.5 ± 0.4	2.9 ± 0.3	0.6 ± 0.2	9.68 ± 0.15	1.76 ± 0.20	8.19 ± 0.25	8.39 ± 0.31
U4-32351	1.9 ± 0.8	2.6 ± 0.2	1.4 ± 0.6	9.56 ± 0.15	1.28 ± 0.24	8.74 ± 0.26	8.49 ± 0.31
U4-16795			1.0 ± 0.1	9.38 ± 0.15	1.81 ± 0.20	8.29 ± 0.21	8.34 ± 0.31
U4-34138	1.2 ± 0.2	5.8 ± 0.4	0.6 ± 0.2	9.41 ± 0.15	1.55 ± 0.21	8.55 ± 0.21	8.41 ± 0.31
U4-28473	1.5 ± 1.2	2.4 ± 0.5	1.2 ± 0.1	9.73 ± 0.15	1.73 ± 0.20	8.16 ± 0.27	8.37 ± 0.31
U4-33135	1.0 ± 2.1	1.5 ± 0.8	0.8 ± 0.2	9.76 ± 0.15	1.36 ± 0.21	8.50 ± 0.29	8.49 ± 0.31
U4-16504	1.0 ± 0.8	3.1 ± 0.8	1.4 ± 0.2	9.46 ± 0.15	1.43 ± 0.21	8.64 ± 0.22	8.44 ± 0.31
U4-34617	0.9 ± 0.3	5.0 ± 0.7	0.3 ± 0.2	9.17 ± 0.15	1.76 ± 0.20	8.40 ± 0.20	8.35 ± 0.31

Notes.
[a] Sérsic indices and half-light radii at 1.6 μm. We do not use U4-16795 because the best-fit Sérsic index reaches the constrained limit of $n = 8$.
[b] Half-light radii at 870 μm.
[c] Stellar mass surface density within a central 1 kpc calculated in stellar mass maps.
[d] SFR surface density within a central 1 kpc calculated from the best-fit exponential models at 870 μm and total SFRs.
[e] Bulge formation timescales to reach the stellar mass surface density of $\log(\Sigma M_{bulge}/M_\odot\,\mathrm{kpc}^{-2}) = 10$ (Equation (3)).
[f] Gas depletion timescales by star formation and outflows (Equation (4)).

$\log(M_{gas}/SFR) = 0.15–0.79\log(1+z) - 0.43\log(sSFR/sSFR_{MS}) + 0.06(\log M_* - 10.5)$, where $sSFR_{MS}$ is the specific SFR on the main-sequence line of Whitaker et al. (2014) at a given redshift and stellar mass. We adopt uncertainties of ±0.24 dex for the $\log(M_{gas}/SFR)$ (Genzel et al. 2015). The gas is partly consumed by star formation and partly ejected by outflows from the central region with comparable rates to SFR, $\eta \times$ SFR ($\eta \sim 1$), especially for massive galaxies (Genzel et al. 2014b). Thus, gas depletion timescales are redefined as

$$\tau_{depl} = \frac{M_{gas}}{SFR(1+\eta)}. \quad (4)$$

The gas depletion timescales are, on average, similar to the bulge formation timescales, $\langle\tau_{bulge}/\tau_{depl}\rangle \sim 1.2$, for the nine galaxies with $R_{1/2,870\,\mu m} < 1.5$ kpc, suggesting that the formation of a dense core does not necessarily require additional gas accretion onto the galaxies.

Next, we look at the kinematic properties for nine galaxies that were observed as part of the KMOS^{3D} program. Six of them have 870 μm size measurements (Table 1). We note that they are all rotation supported ($v_{rot}/\sigma_0 > 3$). Figure 6 shows specific angular momenta as a function of stellar mass for galaxies at $z = 0.8$–2.6 from the KMOS^{3D} survey (Burkert et al. 2016). They span a range of disk angular momenta from local spirals to ellipticals (Fall & Romanowsky 2013). A lower offset at fixed stellar masses suggests that galaxies have lost a significant fraction of their original angular momentum (e.g., major mergers; Naab et al. 2014; Genel et al. 2015) or that they had a small initial angular momentum. We find the specific angular momentum of galaxies with $R_{1/2,870\,\mu m} < 1.5$ kpc to be broadly consistent with a large sample of primarily mass-selected galaxies from the KMOS^{3D} survey. Our result plausibly indicates that these galaxies as a group are not all galaxies with very low angular momentum, either due to large angular momentum loss of the baryonic component or due to a small initial dark matter angular momentum parameter. The compact nuclear dust components we have detected are most likely caused by internal angular momentum redistribution,

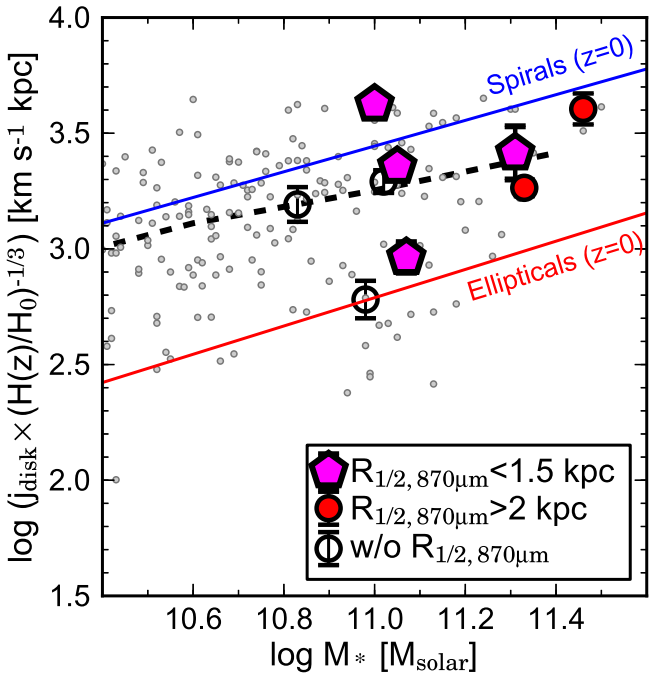

Figure 6. Specific angular momentum of disks vs. stellar mass for our ALMA sample. Magenta pentagons and red circles denote galaxies with $R_{1/2,870\,\mu m} < 1.5$ kpc and with $R_{1/2,870\,\mu m} > 2.0$ kpc, respectively. The kinematic properties are derived from ionized gas. Gray circles indicate the KMOS3D sample of galaxies at $z = 0.8$–2.6, along with their median values in stellar mass bins of 0.4 dex (dashed line). The relations for local spiral and elliptical galaxies are shown by a blue and red solid line, respectively (Fall & Romanowsky 2013). Here, the redshift dependence is removed by multiplying j_{disk} with $H(z)^{1/3}$.

such as has been proposed by recent observations and theoretical studies (Dekel & Burkert 2014; Zolotov et al. 2015; Burkert et al. 2016).

Finally, we speculate that the halo masses inferred from our KMOS observations and a Monte Carlo modeling are $\log(M_{halo}/M_\odot) > 12$ (Burkert et al. 2016). In such massive halos,

infalling gas along cosmic filaments is heated to the halo virial temperature by shocks, and cold gas is not directly supplied to galaxies (e.g., Dekel & Birnboim 2006). Given that the bulge formation timescales are comparable with the gas depletion timescales by central starbursts and outflows, they can naturally quench star formation soon after the dense core is formed. Even if some amount of cold gas accretes onto galaxy disks after cooling, a steep potential by the dense core (morphological quenching) helps galaxies to keep quiescent properties after nuclear starbursts consume all central gas or outflows eject it. Therefore, galaxies with compact dust emission would be a key population for understanding the morphological and star formation evolution from star-forming disks to quiescent spheroids at the massive end of the main sequence.

On the other hand, our observations detect relatively extended dust emission of $R_{1/2,870\,\mu m} > 2$ kpc from the remaining three massive galaxies. Although the bulge formation timescale is longer than the gas depletion timescale, $\tau_{bulge}/\tau_{depl} > 2$, two of them show a high Sérsic index, $n > 2$, in the rest-optical, suggesting that the bulge is already formed. They can directly become large quiescent galaxies after consuming gas, not through the compaction phase (van Dokkum et al. 2015). This mode would become dominant at a later epoch when the number density of optically compact galaxies decreases (Barro et al. 2013).

5. SUMMARY

We have presented 0.″2-resolution 870 μm observations for 25 Hα-selected star-forming galaxies on/around the main sequence at $z = 2.2$ and $z = 2.5$ with ALMA. We have robustly detected the dust continuum emission from 16 galaxies and measured the half-light radii for the best sample of 12 massive galaxies with $\log(M_*/M_\odot) > 11$. In this paper, we have investigated dense core formation in extended star-forming disks and verified the evolutionary scenarios from disk-dominated galaxies to bulge-dominated ones.

1. We have discovered nine massive galaxies associated with extremely compact dust emission with $R_{1/2,870\,\mu m} < 1.5$ kpc. In spite of the compact appearance at 870 μm, they have an extended, rotating disk with $R_{1/2,1.6\,\mu m} = 3.2$ kpc and $n_{1.6\,\mu m} = 1.2$ in the rest-optical. The difference of morphologies between dusty star formation and stars suggests that they would reduce the half-light or half-mass radius by the subsequent star formation and increase the Sérsic index. Given the high completeness in the stellar mass range of $\log(M_*/M_\odot) > 11$, they are likely a common population of massive star-forming galaxies at $z \sim 2$.
2. Galaxies with $R_{1/2,870\,\mu m} < 1.5$ kpc can complete the formation of a dense core in several hundred megayears if the current level of star formation is maintained. This would be reasonable because the bulge formation timescales are comparable with the gas depletion timescales by star formation and nuclear outflows. Therefore, they can naturally quench star formation after the dense core is formed.
3. Three massive star-forming galaxies show somewhat extended dust emission with $R_{1/2,870\,\mu m} > 2.0$ kpc. As two of them already have a cusp profile ($n > 2$) rather than exponential disks, they can evolve into extended quiescent galaxies. This direct pathway is not the norm at $z \sim 2$, but could dominate at later epochs.
4. For our ALMA sample, available integral-field observations of Hα emission with KMOS provide the kinematic parameters of ionized gas such as rotation velocity, local velocity dispersion, and specific angular momentum. They are all rotation-supported disks, and their disk angular momenta are consistent with a large sample of mass-selected star-forming galaxies at $z = 0.8$–2.6 in the KMOS^{3D} survey. Our finding suggests that internal processes are primarily responsible for the bulge formation rather than major mergers.

We thank the anonymous referee, who gave us many useful comments that improved the paper. This paper makes use of the following ALMA data: ADS/JAO.ALMA#2012.1.00245.S and 2013.1.00566.S. ALMA is a partnership of ESO (representing its member states), NSF (USA), and NINS (Japan), together with NRC (Canada), NSC and ASIAA (Taiwan), and KASI (Republic of Korea), in cooperation with the Republic of Chile. The Joint ALMA Observatory is operated by ESO, AUI/NRAO, and NAOJ. We thank the staff at Paranal Observatory for their helpful support. Data analysis was in part carried out on the common-use data analysis computer system at the Astronomy Data Center (ADC) of the National Astronomical Observatory of Japan. K.T. was supported by the ALMA Japan Research Grant of NAOJ Chile Observatory, NAOJ-ALMA-34. This paper is produced as a part of our collaborations through the joint project supported by JSPS and DAAD under the Japan—German Research Cooperative Program. S.I. acknowledges the support of the Netherlands Organization for Scientific Research (NWO) through the Top Grant Project 614.001.403.

REFERENCES

Barro, G., Faber, S. M., Koo, D. C., et al. 2015, ApJ, submitted (arXiv:1509.00469)
Barro, G., Faber, S. M., Pérez-González, P. G., et al. 2013, ApJ, 765, 104
Barro, G., Faber, S. M., Pérez-González, P. G., et al. 2014, ApJ, 791, 52
Barro, G., Kriek, M., Pérez-González, P. G., et al. 2016, ApJL, 827, L32
Bell, E. F., van der Wel, A., Papovich, C., et al. 2012, ApJ, 753, 167
Belli, S., Newman, A. B., & Ellis, R. S. 2015, ApJ, 799, 206
Bouché, N., Dekel, A., Genzel, R., et al. 2010, ApJ, 718, 1001
Bournaud, F., Dekel, A., Teyssier, R., et al. 2011, ApJL, 741, L33
Bower, R. G., Benson, A. J., Malbon, R., et al. 2006, MNRAS, 370, 645
Bruzual, G., & Charlot, S. 2003, MNRAS, 344, 1000
Burkert, A., Förster Schreiber, N. M., Genzel, R., et al. 2016, ApJ, 826, 214
Calzetti, D., Armus, L., Bohlin, R. C., et al. 2000, ApJ, 533, 682
Chabrier, G. 2003, PASP, 115, 763
Croton, D. J., Springel, V., White, S. D. M., et al. 2006, MNRAS, 365, 11
Daddi, E., Dickinson, M., Morrison, G., et al. 2007, ApJ, 670, 156
Davé, R., Finlator, K., & Oppenheimer, B. D. 2012, MNRAS, 421, 98
Davies, R. I., Agudo Berbel, A., Wiezorrek, E., et al. 2013, A&A, 558, A56
Dekel, A., & Birnboim, Y. 2006, MNRAS, 368, 2
Dekel, A., & Burkert, A. 2014, MNRAS, 438, 1870
Dekel, A., Sari, R., & Ceverino, D. 2009, ApJ, 703, 785
Dunlop, J. S., McLure, R. J., Biggs, A. D., et al. 2016, MNRAS, in press (arXiv:1606.00227)
Elbaz, D., Daddi, E., Le Borgne, D., et al. 2007, A&A, 468, 33
Elmegreen, B. G., Bournaud, F., & Elmegreen, D. M. 2008, ApJ, 688, 67
Fall, S. M., & Romanowsky, A. J. 2013, ApJL, 769, L26
Förster Schreiber, N. M., Genzel, R., Bouché, N., et al. 2009, ApJ, 706, 1364
Förster Schreiber, N. M., Genzel, R., Newman, S. F., et al. 2014, ApJ, 787, 38
Genel, S., Fall, S. M., Hernquist, L., et al. 2015, ApJL, 804, L40
Genzel, R., Burkert, A., Bouché, N., et al. 2008, ApJ, 687, 59
Genzel, R., Förster Schreiber, N. M., Lang, P., et al. 2014a, ApJ, 785, 75
Genzel, R., Förster Schreiber, N. M., Rosario, D., et al. 2014b, ApJ, 796, 7
Genzel, R., Newman, S., Jones, T., et al. 2011, ApJ, 733, 101

Genzel, R., Tacconi, L. J., Lutz, D., et al. 2015, ApJ, 800, 20
Grogin, N. A., Kocevski, D. D., Faber, S. M., et al. 2011, ApJS, 197, 35
Ikarashi, S., Ivison, R. J., Caputi, K. I., et al. 2015, ApJ, 810, 133
Ilbert, O., McCracken, H. J., Le Fèvre, O., et al. 2013, A&A, 556, A55
Immeli, A., Samland, M., Gerhard, O., & Westera, P. 2004a, A&A, 413, 547
Immeli, A., Samland, M., Westera, P., & Gerhard, O. 2004b, ApJ, 611, 20
Kashino, D., Silverman, J. D., Rodighiero, G., et al. 2013, ApJL, 777, L8
Kennicutt, R. C., Jr. 1998, ARA&A, 36, 189
Kodama, T., Hayashi, M., Koyama, Y., et al. 2013, in IAU Symp. 295, The Intriguing Life of Massive Galaxies, ed. D. Thomas, A. Pasquali, & I. Ferreras (Cambridge: Cambridge Univ. Press), 74
Koekemoer, A. M., Faber, S. M., Ferguson, H. C., et al. 2011, ApJS, 197, 36
Kriek, M., van Dokkum, P. G., Labbé, I., et al. 2009, ApJ, 700, 221
Lang, P., Wuyts, S., Somerville, R. S., et al. 2014, ApJ, 788, 11
Law, D. R., Steidel, C. C., Erb, D. K., et al. 2009, ApJ, 697, 2057
Lilly, S. J., & Carollo, C. M. 2016, ApJ, 833, 1
Lilly, S. J., Carollo, C. M., Pipino, A., Renzini, A., & Peng, Y. 2013, ApJ, 772, 119
Lindroos, L., Knudsen, K. K., Vlemmings, W., Conway, J., & Martí-Vidal, I. 2015, MNRAS, 446, 3502
Lutz, D., Poglitsch, A., Altieri, B., et al. 2011, A&A, 532, A90
Marchesini, D., van Dokkum, P. G., Förster Schreiber, N. M., et al. 2009, ApJ, 701, 1765
Martig, M., Bournaud, F., Teyssier, R., & Dekel, A. 2009, ApJ, 707, 250
Martí-Vidal, I., Vlemmings, W. H. T., Muller, S., & Casey, S. 2014, A&A, 563, A136
McMullin, J. P., Waters, B., Schiebel, D., Young, W., & Golap, K. 2007, in ASP Conf. Ser. 376, Astronomical Data Analysis Software and Systems XVI, ed. R. A. Shaw, F. Hill, & D. J. Bell (San Francisco, CA: ASP), 127
Mendel, J. T., Saglia, R. P., Bender, R., et al. 2015, ApJL, 804, L4
Mihos, J. C., & Hernquist, L. 1996, ApJ, 464, 641
Momcheva, I. G., Brammer, G. B., van Dokkum, P. G., et al. 2016, ApJS, 225, 27
Mosleh, M., Williams, R. J., Franx, M., et al. 2012, ApJL, 756, L12
Muzzin, A., Marchesini, D., Stefanon, M., et al. 2013, ApJ, 777, 18
Naab, T., Oser, L., Emsellem, E., et al. 2014, MNRAS, 444, 3357
Nelson, E. J., van Dokkum, P. G., Brammer, G., et al. 2012, ApJL, 747, L28
Nelson, E. J., van Dokkum, P. G., Förster Schreiber, N. M., et al. 2016a, ApJ, 828, 27
Nelson, E. J., van Dokkum, P. G., Momcheva, I. G., et al. 2016b, ApJL, 817, L9
Newman, A. B., Ellis, R. S., Bundy, K., & Treu, T. 2012, ApJ, 746, 162
Noeske, K. G., Weiner, B. J., Faber, S. M., et al. 2007, ApJL, 660, L43
Noguchi, M. 1999, ApJ, 514, 77
Onodera, M., Carollo, C. M., Renzini, A., et al. 2015, ApJ, 808, 161
Pannella, M., Carilli, C. L., Daddi, E., et al. 2009, ApJL, 698, L116
Peng, C. Y., Ho, L. C., Impey, C. D., & Rix, H.-W. 2010, AJ, 139, 2097
Piazzo, L., Calzoletti, L., Faustini, F., et al. 2015, MNRAS, 447, 1471
Price, S. H., Kriek, M., Shapley, A. E., et al. 2016, ApJ, 819, 80
Rodighiero, G., Daddi, E., Baronchelli, I., et al. 2011, ApJL, 739, L40
Romanowsky, A. J., & Fall, S. M. 2012, ApJS, 203, 17
Rujopakarn, W., Dunlop, J. S., Rieke, G. H., et al. 2016, ApJ, 833, 12
Shibuya, T., Ouchi, M., & Harikane, Y. 2015, ApJS, 219, 15
Shivaei, I., Reddy, N. A., Shapley, A. E., et al. 2015, ApJ, 815, 98
Simpson, J. M., Smail, I., Swinbank, A. M., et al. 2015, ApJ, 799, 81
Skelton, R. E., Whitaker, K. E., Momcheva, I. G., et al. 2014, ApJS, 214, 24
Stott, J. P., Swinbank, A. M., Johnson, H. L., et al. 2016, MNRAS, 457, 1888
Suzuki, T. L., Kodama, T., Tadaki, K.-i., et al. 2015, ApJ, 806, 208
Swinbank, A. M., Sobral, D., Smail, I., et al. 2012, MNRAS, 426, 935
Tacchella, S., Carollo, C. M., Renzini, A., et al. 2015, Sci, 348, 314
Tacchella, S., Dekel, A., Carollo, C. M., et al. 2016, MNRAS, 458, 242
Tacconi, L. J., Neri, R., Genzel, R., et al. 2013, ApJ, 768, 74
Tadaki, K.-I., Kodama, T., Koyama, Y., et al. 2011, PASJ, 63, 437
Tadaki, K.-I., Kodama, T., Tanaka, I., et al. 2013, ApJ, 778, 114
Tadaki, K.-I., Kohno, K., Kodama, T., et al. 2015, ApJL, 811, L3
Tasca, L. A. M., Le Fèvre, O., Hathi, N. P., et al. 2015, A&A, 581, A54
Toft, S., van Dokkum, P., Franx, M., et al. 2007, ApJ, 671, 285
Trujillo, I., Conselice, C. J., Bundy, K., et al. 2007, MNRAS, 382, 109
van der Wel, A., Bell, E. F., Häussler, B., et al. 2012, ApJS, 203, 24
van der Wel, A., Chang, Y.-Y., Bell, E. F., et al. 2014a, ApJL, 792, L6
van der Wel, A., Franx, M., van Dokkum, P. G., et al. 2014b, ApJ, 788, 28
van Dokkum, P. G., Bezanson, R., van der Wel, A., et al. 2014, ApJ, 791, 45
van Dokkum, P. G., Franx, M., Kriek, M., et al. 2008, ApJL, 677, L5
van Dokkum, P. G., Nelson, E. J., Franx, M., et al. 2015, ApJ, 813, 23
Whitaker, K. E., Franx, M., Bezanson, R., et al. 2015, ApJL, 811, L12
Whitaker, K. E., Franx, M., Leja, J., et al. 2014, ApJ, 795, 104
Whitaker, K. E., van Dokkum, P. G., Brammer, G., et al. 2013, ApJL, 770, L39
Whitaker, K. E., van Dokkum, P. G., Brammer, G., & Franx, M. 2012, ApJL, 754, L29
Wisnioski, E., Förster Schreiber, N. M., Wuyts, S., et al. 2015, ApJ, 799, 209
Wuyts, S., Cox, T. J., Hayward, C. C., et al. 2010, ApJ, 722, 1666
Wuyts, S., Förster Schreiber, N. M., Genzel, R., et al. 2012, ApJ, 753, 114
Wuyts, S., Förster Schreiber, N. M., Lutz, D., et al. 2011a, ApJ, 738, 106
Wuyts, S., Förster Schreiber, N. M., Nelson, E. J., et al. 2013, ApJ, 779, 135
Wuyts, S., Förster Schreiber, N. M., van der Wel, A., et al. 2011b, ApJ, 742, 96
Wuyts, S., Förster Schreiber, N. M., Wisnioski, E., et al. 2016, ApJ, 831, 149
Zolotov, A., Dekel, A., Mandelker, N., et al. 2015, MNRAS, 450, 2327